Progress In Electromagnetics Research C, Vol. 78, 193–208, 2017

A New Method of Stomach Tumor Recognition Based on Ultra Wideband Capsule Endoscopy

Gong Chen*, Ye-Rong Zhang, and Bi-Yun Chen

Abstract—In this paper, a new kind of capsule endoscopy with through-body radar is utilized for the first time. Finite difference time domain (FDTD) method is used to establish an electromagnetic simulation model of stomach. A technique based on the combination of improved back-projection (BP) algorithm and support vector machine (SVM) is proposed to solve the problems of rapidly recognizing tumor shapes in the stomach. In this technique, imaging data can be obtained using the improved BP algorithm and are classified by the SVM. The algorithm must consider the influence of various tissues in the human body: the attenuation of the signal strength of electromagnetic waves, the decrease in speed and the refraction due to the different permittivity between the different organs of the body. These factors will eventually lead to image offset, and even generate a virtual image. It is effective to refrain the displacement of image with modifying the time element of the imaging algorithm by iteration. Simulation results based on data from the model verify its feasibility and validity. Results further demonstrate that the resolution is extremely high. Tumor shapes, which have different sizes, positions, and quantities, can be reconstructed using this approach. When the data are contaminated by noises, the tumor shape in the stomach can still be suitably predicted, which demonstrates the robustness of the method. Finally, classification accuracy analysis for different sampling distances and sampling intervals shows that the effects of changing the distance and intervals on shape recognition are limited. The classification accuracy can also be improved by decreasing the sampling intervals or increasing the sampling distance.

1. INTRODUCTION

Inverse scattering problem in electromagnetic devices refers to the use of radar signals from outside the scatter to invert the electromagnetic characteristics of the scatter; the word "scattering" is a generalized concept, which includes reflection, refraction, diffraction, transmission, and scattering [1]. This theory is widely applied in different areas, such as microwave imaging techniques [2–5], medical imaging, seismology, ground penetrating radars, and geophysical exploration.

The gastrointestinal (GI) tract is a hollow and muscular conduit from the mouth to the anus. GI tract-related cancers, such as gastric, esophageal, and colon cancers, have been ranked as the third, fourth, and fifth causes of male cancer deaths, respectively, whereas they have been ranked as the fourth, fifth, and sixth causes of female cancer deaths, respectively, in Hong Kong in 2014 [6]. Tumors in the GI tract largely threaten human health.

A novel technique of endoscopy called wireless capsule endoscopy (WCE) was introduced in 2000 to diagnose GI tract cancers [7–9]. It consists of a camera with a short focal length, light source, and radio transmitter. After the capsule is swallowed by a patient, it relies on the self peristalsis of the human GI tract for movement through the esophagus and stomach before finally draining out of the

Received 5 August 2017, Accepted 7 October 2017, Scheduled 14 October 2017
* Corresponding author: Gong Chen (chengong9269@sina.com).
The authors are with the College of Electronics Science and Technology, Nanjing University of Posts and Telecommunications, Nanjing 210003, China.

body. The process took more than 8 hours. The camera takes photos of the GI tract that produce thousands of images in each examination. Spending two or more hours to review all the images would be time consuming for physicians. The chances of committing errors and misdiagnoses increase because the physicians are focused on a small part of the field for a long time. Gono et al. proposed the narrow band image technology to overcome these drawbacks of traditional endoscope [10–12]. Atasoy et al. [13] proposed an MRF-based matching technique that incorporates region-based similarities and spatial correlations of neighboring regions that are applied to narrow-band endoscopy for targeted optical biopsy. Recently, Li and Meng studied a computerized tumor detection system for WCE images, which exploits textural features and support vector machine (SVM)-based feature selection [14–17].

The aforementioned studies have solved the detection of bleeding and ulcer in WCE images but have not achieved real-time imaging. Therefore, a new type of capsule endoscopy which called ultra wideband capsule endoscopy with through-body radar is used in the present study for the first time. This paper breaks the traditional method of carrying camera in capsule endoscope, but adds ultra wideband radar in new capsule endoscope, so as to achieve the purpose of real-time imaging of stomach tumors. A technique based on the combination of improved back projection (BP) algorithm and SVM is proposed. This paper simulates the propagation model of electromagnetic wave in human body. In order to eliminate the morbidity and nonlinearity in human imaging, the time element in BP algorithm is modified. In this technique, imaging data can be obtained by utilizing the improved BP algorithm and classified by SVM. Based on efficiency, improved BP algorithm requires 40 s to 60 s on the computer with Intel Core i5 CPU. After obtaining characteristic data, prediction process of SVM based on improved BP algorithm requires only 1 s. Therefore, the method on the combination of SVM and improved BP algorithm not only can recognize the location and shape of the tumors, but also can meet requirements of real-time detection. It can be employed for tumor positioning and help clinicians make decisions.

2. PROPAGATION MODEL OF ELECTROMAGNETIC WAVE IN HUMAN BODY

Ultra-wideband radar has three basic modes, including short pulse, frequency modulation and frequency step modulation. The fractional bandwidth of ultra wideband short pulse radar is greater than 0.25. It has short launch range, just a few nanoseconds, and excellent range resolution. For ultra short range detection, it has good transmission characteristics. It has obvious advantages in human body imaging, so the UWB short pulse radar is used in this paper.

As shown in Figure 1, the thickness of the stomach is d_w, and relative dielectric constant is ε_r.

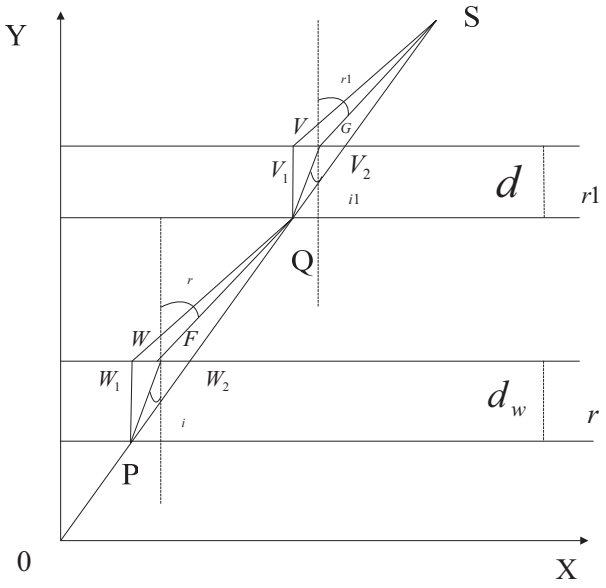

Figure 1. Refraction model.

The thickness of the abdominal muscles is d, and relative dielectric constant is ε_{r1}. In rectangular coordinates X-0-Y, the position of the capsule emission source is the coordinate origin; the position of the receiving antenna is $S(s_x, s_y)$; the intersection of the electromagnetic wave and the stomach is $P(p_x, p_y)$; the refracted point is $W(w_x, w_y)$; the coordinates of F is $F(f_x, f_y)$, $f_x = q_x - w_x$, $f_y = q_y - w_y$. The intersection of electromagnetic waves with the abdominal cavity is $Q(q_x, q_y)$; the refracted point is $V(v_x, v_y)$; the coordinates of G is (g_x, g_y), $g_x = s_x - v_x$, $g_y = s_y - v_y$.

The propagation path of electromagnetic wave in the stomach is calculated by the iteration method. Two extreme cases are considered: assuming that the stomach wall is air, the relative dielectric constant is $\varepsilon_r = 1$. Then there is no refraction in the electromagnetic wave, and its propagation path is straight OPQ. The intersection of the electromagnetic wave and the stomach is $W_2(w_{2x}, p_y + d_w)$. It is also assumed that the relative dielectric constant of the gastric wall is infinite. The propagation path of electromagnetic wave is approximately perpendicular to the stomach wall. The propagation path is OPW_1Q, and the intersection point is $W_1 w_{1x}, p_y + d_w)$. Since the electromagnetic wave has to satisfy the law of refraction on the surface of two kinds of dielectric decomposition, it can be seen that $w_1 < w < w_2$. The geometric relationship between the incident angle and refraction angle is as follows:

$$\sin(\theta_i) = \frac{w_x - p_x}{\sqrt{(w_x - p_x)^2 + (w_y - p_y)^2}} \tag{1}$$

$$\sin(\theta_r) = \frac{f_x}{\sqrt{f_x^2 + f_y^2}} \tag{2}$$

$$k = \frac{\sin(\theta_i)}{\sin(\theta_r)} \tag{3}$$

where $f_x = q_x - w_x$, $f_y = q_y - w_y$; refractive index is k; incident angle is θ_i; refraction angle is θ_r.

The actual refractive index $W(w_x, w_y)$ is obtained by iterative method:

(a) Let the initial value of w_x be the midpoint w_0 of the interval (w_{x1}, w_{x2}), k is obtained by Equations (1), (2) and (3).

(b) k is compared with the relative dielectric constant of gastric wall tissue ε_r, if $k < \varepsilon_r$, take the midpoint of the interval (w_{x1}, w_0), if $k > \varepsilon_r$, take the midpoint of the interval (w_0, w_{x2}).

(c) Repeat steps (a) and (b) until $k = \varepsilon_r$, then the iteration stops. Finally, the refraction point $W(w_x, w_y)$ is obtained.

Similarly, the refractive index of the electromagnetic wave in the abdominal muscles ε_{r1} can be calculated in the manner described above.

The propagation distance of electromagnetic wave in the gastric wall is l_1. The propagation distance in non-human tissues is $l_2 + l_3 + l_4$. The propagation distance in the abdominal muscles is l_5. The propagation time of an electromagnetic wave from the transmitter to the receiver is:

$$\begin{aligned} t &= \frac{l_1}{v} + \frac{l_2 + l_3 + l_4}{c} + \frac{l_5}{v} \\ &= \frac{\sqrt{\varepsilon_r} l_1}{c} + \frac{l_2 + l_3 + l_4}{c} + \frac{\sqrt{\varepsilon_{r1}} l_5}{c} \\ &= \frac{\sqrt{\varepsilon_r} l_1 + \sqrt{\varepsilon_{r1}} l_5 + l_2 + l_3 + l_4}{c} \\ &= \frac{d_{eff}}{c} \end{aligned} \tag{4}$$

where d_{eff} is the effective propagation distance of electromagnetic wave, c the speed of light in vacuum, v the speed at which electromagnetic waves travel through the stomach wall and abdominal muscles, ε_r the relative dielectric constant of the gastric wall, and ε_{r1} the relative permittivity of the abdominal cavity.

3. BASIC PRINCIPLE OF SVM

3.1. SVM

SVM is a state-of-the-art technique applied to classification and demonstrates better accuracy and computational advantages over several other traditional classification approaches [18–21].

SVM is a linear classifier. Its purpose in this study is to select the classified hyperplane, which can maximize the margin that separates the two sample classes in a binary classifier. First, we define a new set of labeled patterns called the training set. Let $\{(x_i, y_i),\ i = 1, 2, \ldots, l\}$ be such a set, where $x_i \in R^n$ is the input information, $y_i \in \{1, -1\}$ the output information of the category of target, and l the number of training samples. Presumably, we introduce a slack variable ξ_i, ξ_i^* for compatibility. Suppose that all the data are fitted in a linear function with accuracy ε. The optimization problem can then be expressed in the following form:

$$\min\left(\frac{1}{2}\|w\|^2 + C\sum_{i=1}^{l}(\xi_i + \xi_i^*)\right), \tag{5}$$

which is subject to the following:

$$\begin{aligned} &((w \cdot x_i) + b) - y_i \le \xi_i + \varepsilon, \quad \xi_i \ge 0\ (i = 1, 2, \ldots, l) \\ &y_i - ((w \cdot x_i) + b) \le \xi_i^* + \varepsilon, \quad \xi_i^* \ge 0\ (i = 1, 2, \ldots, l)' \end{aligned} \tag{6}$$

where w and b are the weight vector and parameter of the decision function, respectively. $C\sum_{i=1}^{l}(\xi_i + \xi_i^*)$ is the loss function, and C is the penalty parameter.

When SVM are adopted to solve the regression problem, the loss function is introduced to detect the error between the fitting and target values. The loss functions mainly include Quadratic, Laplace, Huber, and ε-insensitive ones.

The loss function used in this study is ε-insensitive with a specific form presented as follows:

$$c(f(x) - y) = \begin{cases} 0 & \text{if } |f(x) - y| \le \varepsilon \\ |f(x) - y| - \varepsilon & \text{otherwise.} \end{cases} \tag{7}$$

Assume that all data are error free in accuracy, so the linear function is utilized to fit them. ε represents accuracy, and y is the actual function value. Given the Lagrange method, the dual-version of the aforementioned problem corresponds to the solution of the following quadratic program:

$$\max\left(\frac{1}{2}\sum_{i=1}^{l}\sum_{j=1}^{l} y_i y_j \alpha_i \alpha_j < \phi(x) \cdot \phi(x_i) > -\sum_{j=1}^{l}\alpha_j\right), \tag{8}$$

which is subject to the following:

$$\sum_{i=1}^{l} y_i \alpha_i = 0, \quad 0 \le \alpha_i \le C\ (i = 1, 2, \ldots, l), \tag{9}$$

where α_i is the Lagrange coefficient, and C is the penalty parameter.

The corresponding decision function can be written as follows:

$$\zeta = \operatorname{sgn}\left(\sum_{i=1}^{j}\alpha_i y_i \langle z_i, z\rangle + b\right), \tag{10}$$

where $\langle \bullet, \bullet \rangle$ is the operation symbol of the inner product.

In the detection of human body images, the relationship between the target information and receiving signal is no longer linear because of the actions of the human body. This condition belongs to linearly non-separable problems in SVM recognition [22–25]. Thus, the nonlinear problem in the low dimensional space is mapped into a linear problem in the high dimensional space by the non-linearity transformation to solve this problem. We determine the unique optimal hyperplane, which can set the

highest degree of separation for the two groups of sample data. We then calculate $z_i^{'}$ and inner product $z^{'}$ from the solution of Eq. (10) in the high dimensional space, where z_i' and z' are the vectors in the said space. However, we only know the vector in the low dimensional space. Thus, we utilize the Hilbert transform to calculate the inner product of the vector in the low dimensional space to replace the inner product in the high dimensional space with kernel functions that satisfy the Mercer condition [26–29]. The kernel function can be written in the following form:

$$K(z_i \cdot z) = \langle z_i', z' \rangle \tag{11}$$

It does not have to determine the detailed mapping relationship of z_i while avoiding the problem of curse of dimensionality. Thus, it solves the ingenious problem of inner product operation in high dimensional space. At this point, the decision function can be written as follows:

$$\zeta = \text{sgn}\left(\sum_{i=1}^{l} \alpha_i y_i K(z_i, z) + b\right) \tag{12}$$

We can obtain a signed value when we enter a new variable z by calculating Eq. (12). This singed value represents the SVM classification of the input z.

3.2. Tumor Recognition Method Based on SVM

Given that the electrical parameters (dielectric constant and electrical conductivity) of healthy and cancer cells are different, they can be classified into two types: healthy cells are negative, whereas cancer cells are positive. SVM suitably performs in binary classification. The simulation data is obtained by the Finite difference time domain (FDTD) method [30–34]. These field values are used as characteristic data of the SVM method. Each mesh that corresponds to cancer cells or healthy cells is labeled as positive or negative. The feature data and default category labels correspond to the SVM input and output, respectively. When tumors present a positive signal, the label is 1. When healthy cells exhibit a negative signal, the label is 0. The SVM input and output have a one-to-one mapping relationship. Therefore, we must determine the characteristic value of each mesh. The flow of the improved BP algorithm [35, 36] is presented as follows:

1) Imaging area is divided into a certain mesh intervals.
2) For each mesh, round-trip delay from transmitter to receiver is computed as follows:

$$t(n) = \frac{R(n)}{v}, \tag{13}$$

   where $R(n)$ represents the path from receiver to capsule. Propagation path is no longer a straight line because of refraction when electromagnetic waves spread throughout the human body. Therefore, effective path d_{eff} must be first calculated in experiments by Equation (4) in Section 2. V corresponds to actual propagation velocity of electromagnetic wave in the human body.
3) Electric field value in position of the receiver is recorded.
4) Steps 1 to 3 are repeated for each mesh.
5) Magnitude of each mesh is calculated in Step 3 and is added as follows:

$$e(x, z) = \sum_{n} e(t(n)). \tag{14}$$

Thus, the amplitude value of each mesh is obtained. The scattering echoes of the tumors, marked as E_s, are then calculated by the background subtraction method. First, the model is simulated in the non-tumor condition in the stomach. We then record the radar signal on all receiver antennas. Second, we only add a tumor model into the stomach model and do not change the other parameter settings. The model is simulated again in this scenario. We record the radar signal on all receiver antennas again. The receiving signal of the tumor itself is obtained by subtracting the first recorded signal from the second recorded signal.

For each mesh, the feature vector E_s is used as the input, and the corresponding category label, marked as ζ, is employed as the output. The data (E_S, ζ) are divided into two parts through the

evaluation system of the training sample data of SVM to obtain the training model. We utilize the training model to forecast data by intelligent evaluation and analysis, as well as obtain the category label of the corresponding position. The position of tumors and healthy cells are distinguished based on the category label to realize the localization and recognition of the tumors.

4. ESTABLISHMENT OF SVM MODEL

This study uses the SVM toolbox developed by Professor Lin Zhiren of Taiwan University to forecast classification accuracy. A total of 364 pixels are selected as training samples, including a certain number of positive samples. Appropriate classifier, kernel function, and normalization methods are selected according to results of several experiments.

Two categories of classifiers, namely, C-SVC and V-SVC, can be selected when SVM is considered as a classifier. Improved BP algorithm is used to predict radar data using the two classifiers. After training, classification accuracies reach 88.674% and 85.321% for C-SVC and V-SVC, respectively. Accuracy rate of C-SVC is higher than that of V-SVC by 3.353%. Thus, C-SVC classifier is selected to train and predict data.

Choice of kernel function significantly affects classification results of SVM. SVM toolbox presents four kinds of kernel function: linear kernel function, polynomial kernel function, radial basis kernel function (RBF), and sigmoid kernel function. SVM toolbox is used to train and predict the data obtained by improved BP algorithm with the four kinds of kernel functions. Classification accuracies of the four kernel functions total are 67.745%, 64.823%, 88.674%, and 50.015%, respectively. Thus, RBF is selected for the SVM model.

This section investigates the influence of normalization of feature data on classification accuracy. Radar data obtained by BP algorithm are normalized by $[-1, 1]$, [0, 1] or non-normalized. Classification accuracies of the three methods reach 88.651%, 88.674%, and 81.962%. Thus, [0, 1] normalization can achieve the best classification results based on presented data.

Penalty parameter C and the parameter δ^2 in RBF can be obtained by optimization of genetic algorithms or networks. As stomach tumor imaging requires real-time imaging, longer delay results in poorer disease prognosis. Therefore, this paper adopts a network optimization method with shorter computation time.

According to machine type classifications, kernel functions, normalization, and parameter selection tests, high classification accuracy in obtaining parameters of C and δ^2 can be achieved with the use of C-SVC classification, RBF, [0, 1] normalization, and network optimization method. Radar data obtained by improved BP algorithm are trained to obtain the SVM model, namely, modelBP. Then, this model is used for subsequent experiments.

5. EXPERIMENTS

5.1. Establishment of the Gastric Tumor Model

The stomach model is shown in Figure 2. The length of the abdominal cavity is 20 cm, whereas its width is 12.5 cm. The relative dielectric constant and electrical conductivity of the abdominal cavity are 36 and 7 S/m, respectively. A circular tumor model with a diameter of 1 cm in the site of the coordinate (0 cm, 4 cm) is obtained. The relative dielectric constant of the tumor is 50, and its electrical conductivity is 4 S/m. The signal source is (0 cm, 0 cm) in a coordinate system. The receiver antenna is placed close to the outer side of the abdomen. A receiver antenna is arranged in the X direction every 0.5 cm. The aperture length is 22 cm, and the antenna number is 45. The transmitting signal is a sine-modulated Gauss pulse with a center frequency of 4 GHz and width of 0.6 ns. The frequency and time domain waveforms of the signal are shown in Figures 3 and 4, respectively.

The space interval of the FDTD is $d_x = d_y = 1$ mm, and the time interval is $dt = 19.25 \times 10^{-12}$. The calculation area is surrounded by a perfect matched layer absorbing boundary.

The imaging area is divided into a 400×300 mesh to improve the accuracy of target recognition. The feature vector is obtained according to the BP algorithm. The samples are then trained by the LibSVM toolbox. This condition means that 120,000 samples contain 377 positive samples and 119,623 negative

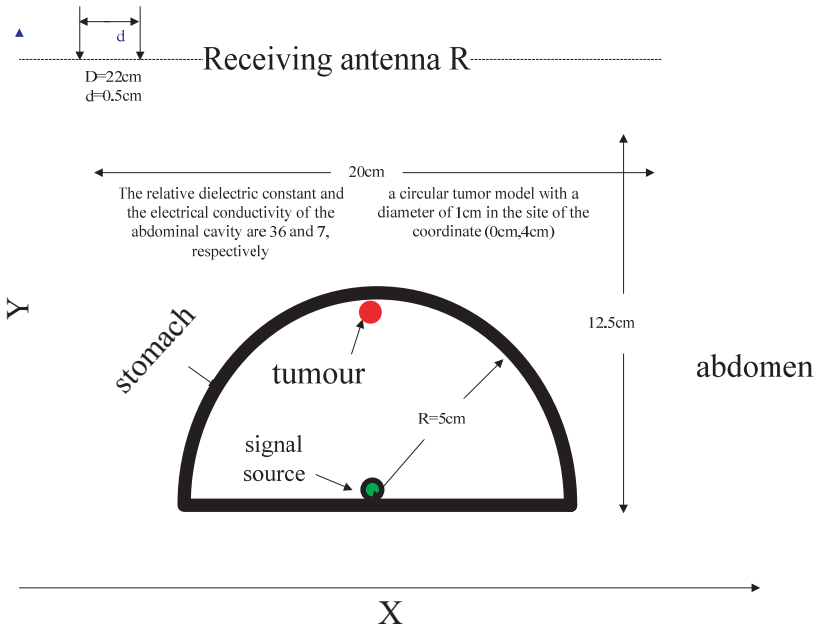

Figure 2. Stomach model.

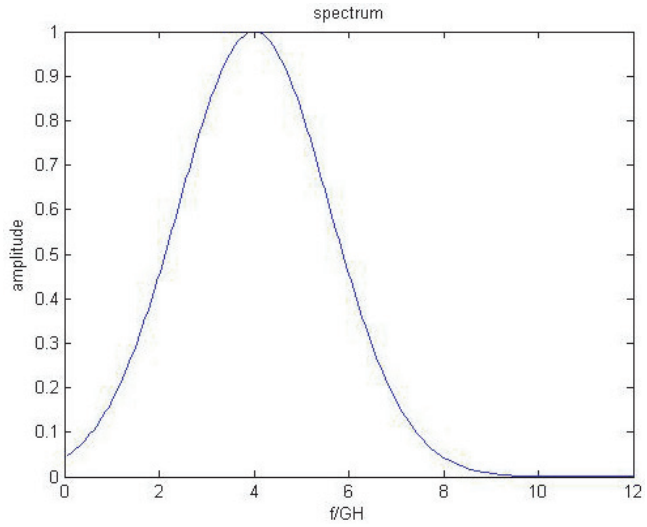

Figure 3. Frequency domain waveform of the transmitted signal.

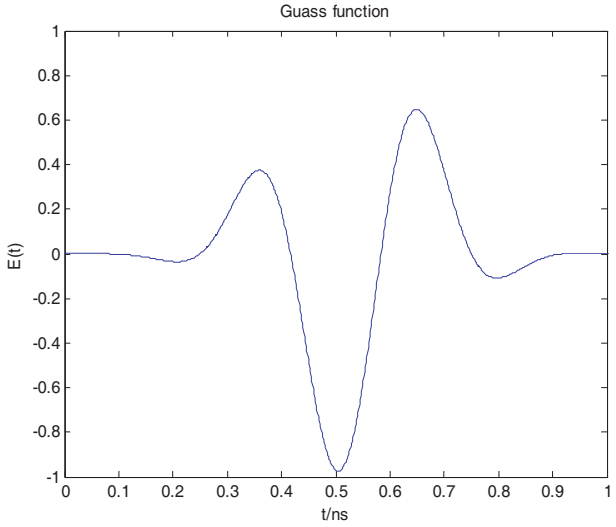

Figure 4. Time domain waveform of the transmitted signal.

samples. A total of 364 data samples, which must include the target information, are selected as the training set. After the training is completed, the training model and receiver operating characteristics (ROC) are obtained. The ROC curve is shown in Figure 5. The classifier has proper classification ability for positive and negative categories as shown in the said figure.

The training model is utilized to predict the entire imaging area. The positive and negative classification accuracy values are 88.674% and 99.964%, respectively. The label of the positive class is 1, whereas the label of the negative class is 0. The classification accuracy of the negative class is extremely high, which indicates that the ability to predict the medium is excellent. The classification accuracy of the positive class is slightly lower, but it can also meet the requirements of stomach imaging. Figure 6 shows the 2D image map formed by the electric field intensity. Figure 7 shows the 3D image map. Figure 8 shows the image map formed by the prediction of the category labels. The red outline

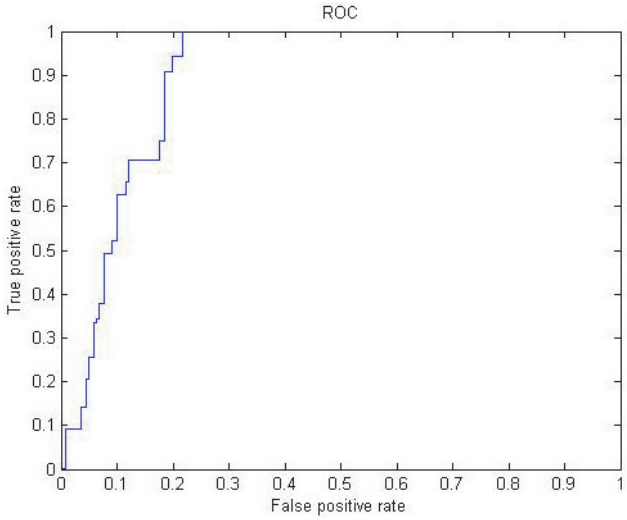

Figure 5. ROC curve.

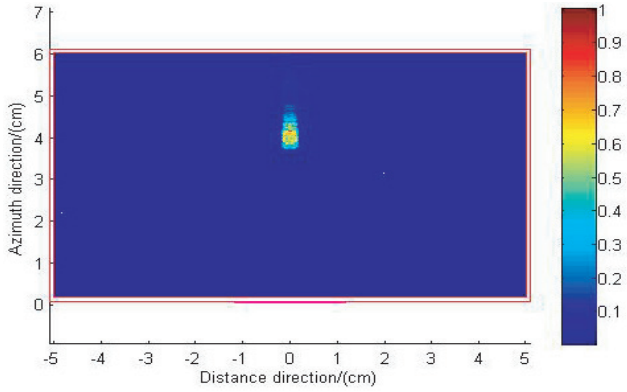

Figure 6. Imaging results by the electric field intensity.

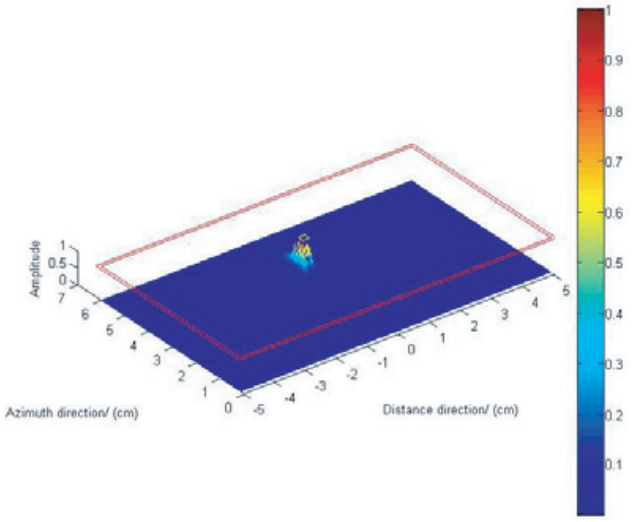

Figure 7. 3D imaging results by the electric field intensity.

indicates the skin of the human body. Red inner frame express the abdomen of human body. The golden box indicates the location of the tumor.

The color block in Figure 8 is the actual location of the tumor target. The actual position and imaging position are relatively consistent. The accurate location of the target is successfully obtained. A virtual shadow exists in the grayscale map of the electric field intensity. The prediction method based on SVM not only eliminates the virtual shadow effectively, but also retains most of the target information. The tumor target information can be predicted when the classification accuracy reaches a certain degree (i.e., the shape of the tumor target has a certain ability to be identified). The classification accuracy of the positive class in this study is 88.674%. The shape and position of the tumor target can be judged properly.

Figure 9 shows the amplitude distribution of the tumor signal in azimuth direction. Figure 10 shows the amplitude distribution of the tumor signal in distance direction. As can be seen from Figures 9 and 10, the peak points are near the actual location of the tumor (0 cm, 4 cm) and achieve very good distance direction resolution and azimuth direction resolution.

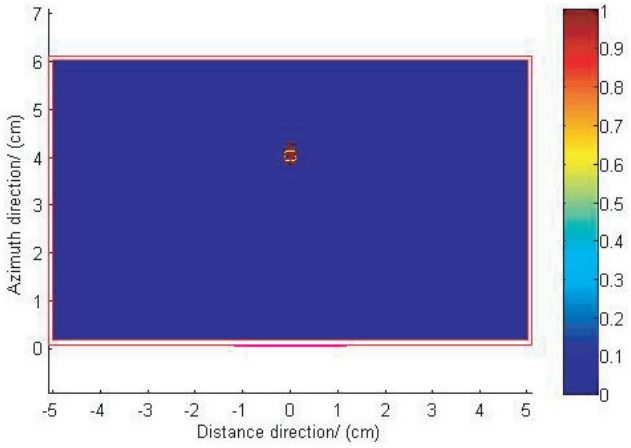

Figure 8. Imaging results by the prediction of the category labels.

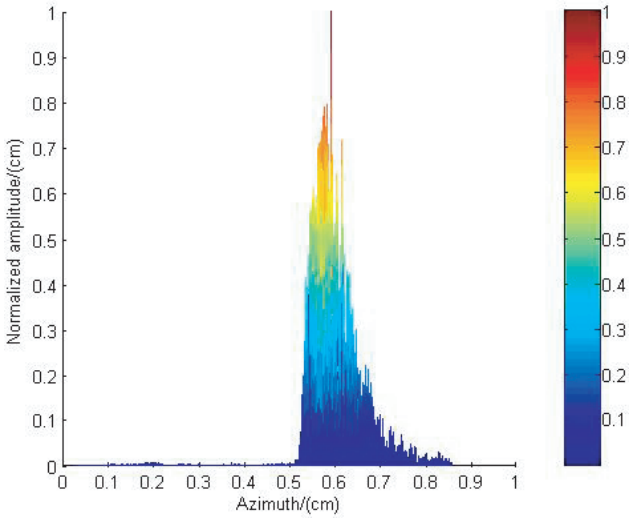

Figure 9. Azimuth direction amplitude distribution.

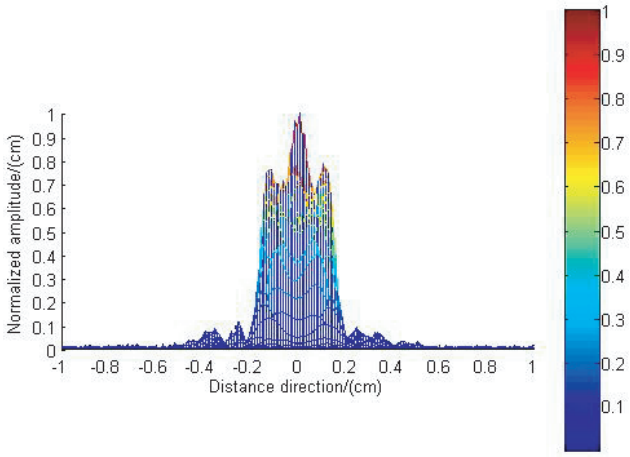

Figure 10. Distance direction amplitude distribution.

Figure 11 shows the distribution of the category labels of the predicted tumor targets in the distance and azimuth directions. In particular, it represents the resolution of the range and azimuth directions, respectively. The tumor position and size are largely consistent with the actual size, which indicates that the distance resolution is extremely high. The azimuth resolution is slightly worse, and some discontinuous phenomena are observed. These conditions will affect the judgment of the target size. It can sometimes be mistaken for multiple goals. The larger the target size, the more significant the impact to the judgment on the target size. Therefore, SVM is highly suitable for the study of gastric rumor imaging.

5.2. Reconstruction of Tumor Models in Different Patients

We obtained a training model of gastric cancer in Section 2.1. This model is then used to predict the different shapes, sizes, locations, and quantities of tumor targets. Given the simulation model in Section 3.1, only the size, location, quantity, and shape of the tumor target are changed:

1) Rectangular shape of the tumor with center coordinates of (3.2 cm, 4.4 cm), length of 1 cm, and width of 0.3 cm;

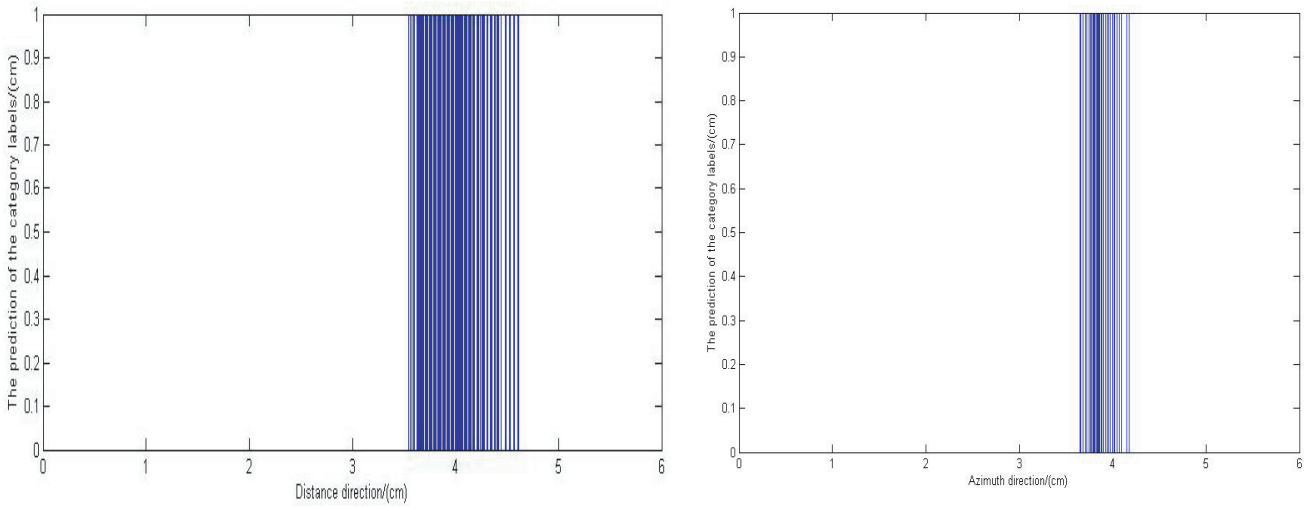

(a) (b)

Figure 11. Resolution of the tumor target. (a) Distance direction. (b) Azimuth direction.

2) Circular tumor shape with center coordinates of (3.5 cm, 3.2 cm) and diameter of 0.8 cm;
3) Square shape of the tumor with center coordinates of (4.2 cm, 2.8 cm) and length of 0.5 cm;
4) Two tumors are detected in the stomach, whose locations, sizes, and shapes are the same as those of Eqs. (1) and (3).

The simulation results are shown in Figures 12 and 13. The said figures show that the prediction results of the SVM and real model are all largely similar in terms of position, shapes, quantities, and sizes. However, virtual shadows exist for multiple tumor targets as shown in Figures 12(c) and 12(d). This phenomenon is related to the improved BP algorithm. In this algorithm, when the target is excessively long in the distance distribution, the signal will be blocked by its front part. Hence, the latter part of the information cannot be obtained, and the imaging effect becomes poor. The distance resolution can be increased by the increasing signal bandwidth. However, this condition will create more shadows and bring more negative effects. Nevertheless, the original shape and position of the target can still be determined. The improved BP algorithm requires 40 s to 60 s based on the algorithm efficiency. After obtaining characteristic data, the SVM prediction based on the algorithm lasts for 1 s. Thus, the method based on the combination of SVM and improved BP algorithm can meet the requirements of real-time detection.

5.3. Signal Polluted by the Noises

The predicted results are based on noise-free conditions. Nevertheless, the data collection process is bound to have noise pollution. Thus, we have to study the signal with the noise.

Table 1 shows the use of the training model to predict the signal of noise pollution. After the addition of different SNR noises, the classification accuracy levels of the positive and negative classes in the imaging area are obtained. The said table shows that the classification accuracy is basically unchanged with the increase in the SNR. This condition shows that the effect of noise pollution on the imaging results is relatively limited. In the imaging region class, the classification accuracy of the negative class is especially high, and the error is 3 bits after the decimal point. This scenario is due to the number of negative class samples being much larger than that of the positive class. The classification accuracy of the positive class is slightly lower, especially the circular tumor, which is related to the input data. However, suitable recognition is still obtained.

The relative root mean square error (RMSE) of the abscissa and ordinate of the tumor center is

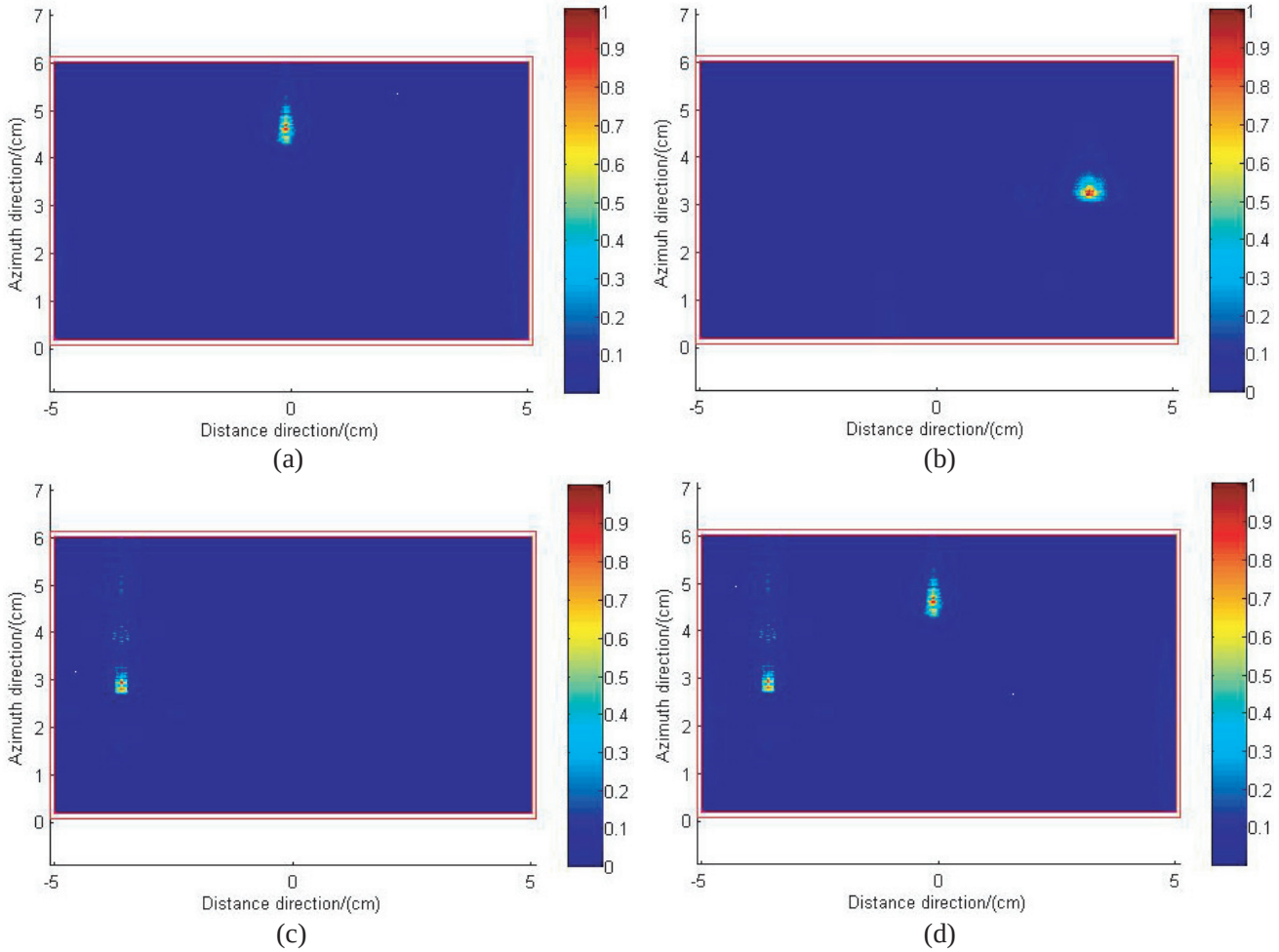

Figure 12. Tumor imaging in different scenarios by the improved BP algorithm. (a) Rectangle tumor imaging based on the improved BP algorithm. (b) Circular tumor imaging based on the improved BP algorithm. (c) Square tumor imaging based on the improved BP algorithm. (d) Imaging of two tumors based on the improved BP algorithm.

Table 1. Classification accuracy of the signal after the noise addition.

SNR/dB		5	30	50	No noise
Square	Imaging area	99.937%	99.935%	99.934%	99.937%
	Negative	99.815%	99.814%	99.812%	99.815%
	Positive	87.987%	88.323%	88.432%	88.674%
Circular	Imaging area	99.238%	99.237%	99.234%	99.241%
	Negative	99.801%	99.798%	99.795%	99.804%
	Positive	46.213%	45.806%	45.684%	46.353%
Rectangle	Imaging area	99.578%	99.572%	99.567%	99.586%
	Negative	99.476%	99.469%	99.465%	99.489%
	Positive	88.642%	88.619%	88.573%	88.661%
Two tumors	Imaging area	99.625%	99.618%	99.609%	99.625%
	Negative	99.574%	99.568%	99.563%	99.575%
	Positive	89.123%	89.076%	89.055%	89.125%

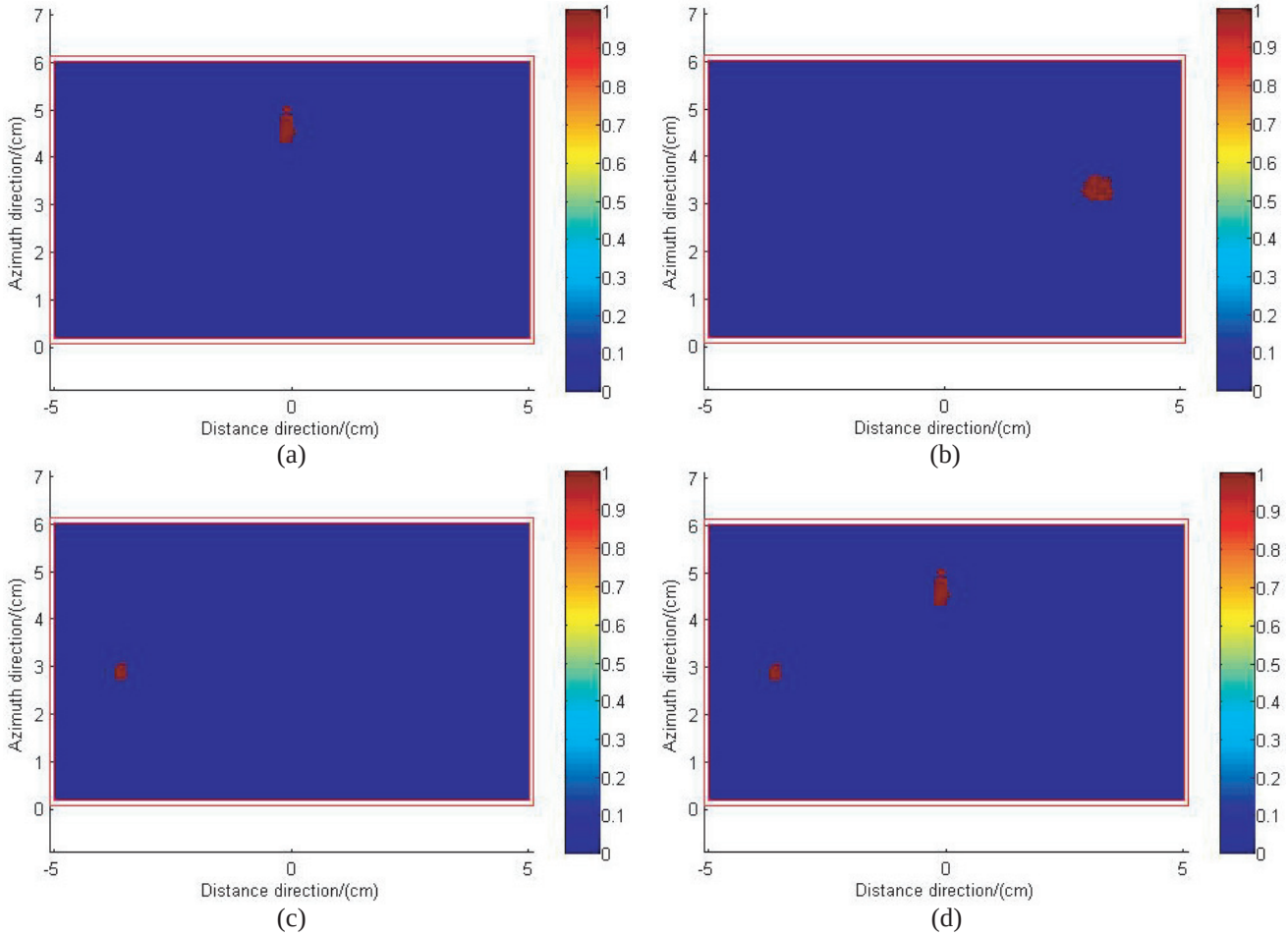

Figure 13. Tumor imaging in different scenarios by SVM. (a) Rectangle tumor target recognition imaging by SVM based on the improved BP algorithm. (b) Circular tumor target recognition imaging by SVM based on the improved BP algorithm. (c) Square tumor target recognition imaging by SVM based on the improved BP algorithm. (d) Target recognition imaging of two tumors by SVM based on the improved BP algorithm.

defined as follows:

$$e_{RMS,x} = \sqrt{\frac{1}{N}\sum_{i=1}^{N}\left(\frac{x_{iact} - x_{ipre}}{l_x}\right)^2}$$
$$e_{RMS,x} = \sqrt{\frac{1}{N}\sum_{i=1}^{N}\left(\frac{y_{iact} - y_{ipre}}{l_y}\right)^2} \quad (15)$$

where (x_{iact}, y_{iact}) is the actual location of the tumor target, (x_{ipre}, y_{ipre}) is the predictive location of the tumor target, l_x and l_y are the model length and width, and N is the number of the test samples.

The proposed method can localize stomach tumors even at low SNR, as shown in Figure 14. As SNR increases, RMSE decreases, and positioning effect improves (i.e., this method is robust).

This section predicts the signal with noise pollution using by the no-noise model. The classification results are basically the same, which shows that the method is robust.

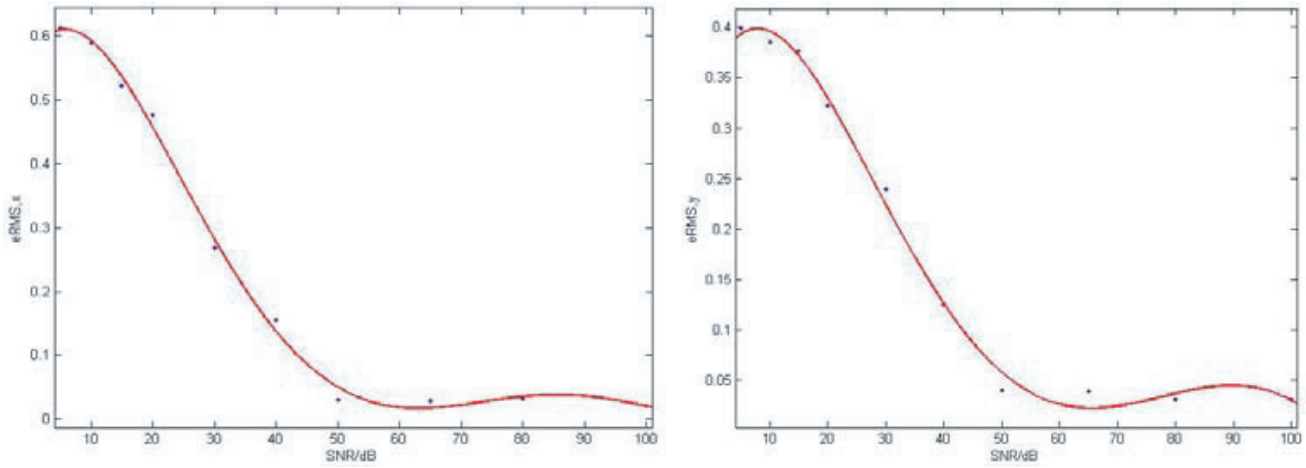

(a) (b)

Figure 14. Tumor target location prediction results of the relation between RMSE and SNR: (a) abscissa, (b) ordinate.

5.4. Effect on the Classification Accuracy of the Sampling Interval and Distance

When the sampling interval and distance are different, the collected data will also be different. The following cases are considered:

1) The sampling distance is 45 cm, and the sampling interval is 0.5 cm;
2) The sampling distance is 9 cm, and the sampling interval is 2.5 cm (the sampling length is constant, whereas the sampling interval is increased 5 times);
3) The sampling distance is 22 cm, and the sampling interval is 0.5 cm (the sampling length is decreased by half, whereas the sampling interval is constant);

Table 2 shows that with the change in sampling interval and distance, the prediction results are different. The classification accuracy of the positive class shows that case 1 has the highest accuracy, case 2 has the lowest accuracy, and case 3 is in the middle. These results mean that the classification accuracy can be improved by decreasing the sampling intervals or increasing the sampling distance.

Table 2. Classification accuracy of different sampling distances and intervals.

Classification accuracy		Imaging area	Negative	Positive
Square	Case 1	99.937%	99.815%	88.674%
	Case 2	99.942%	99.841%	79.523%
	Case 3	99.928%	99.802%	86.549%
Circular	Case 1	99.241%	99.804%	46.353%
	Case 2	99.132%	99.909%	36.957%
	Case 3	99.134%	99.886%	37.562%
Rectangle	Case 1	99.586%	99.489%	88.661%
	Case 2	98.927%	98.842%	65.761%
	Case 3	99.486%	99.471%	79.826%
Two tumors	Case 1	99.625%	99.575%	89.125%
	Case 2	99.112%	99.218%	66.204%
	Case 3	99.623%	99.748%	81.157%

Furthermore, the effect of increasing the sampling distance on the classification is smaller than that of decreasing the sampling intervals. The error rate of the classification accuracy is within 20% in all of the aforementioned scenarios. The difference is insignificant, And the robustness of the method is proved again.

The relationship between the RMSE and sample location number R is shown in Figure 15.

With the increase in sampling location, the prediction error decreases, and the prediction performance improves. Results show that the detection accuracy of a gastric tumor can be improved by increasing the number of receiving antennas.

Therefore, the stability of the method, which uses SVM to predict the tumor target, is demonstrated in different shapes, quantities, positions, SNRs, sampling intervals, and sampling distances. SVM is a learning machine for small sample data. The operation time in determining characteristic data is less than 1 s regardless of the condition, which provides the possibility of real-time tumor imaging.

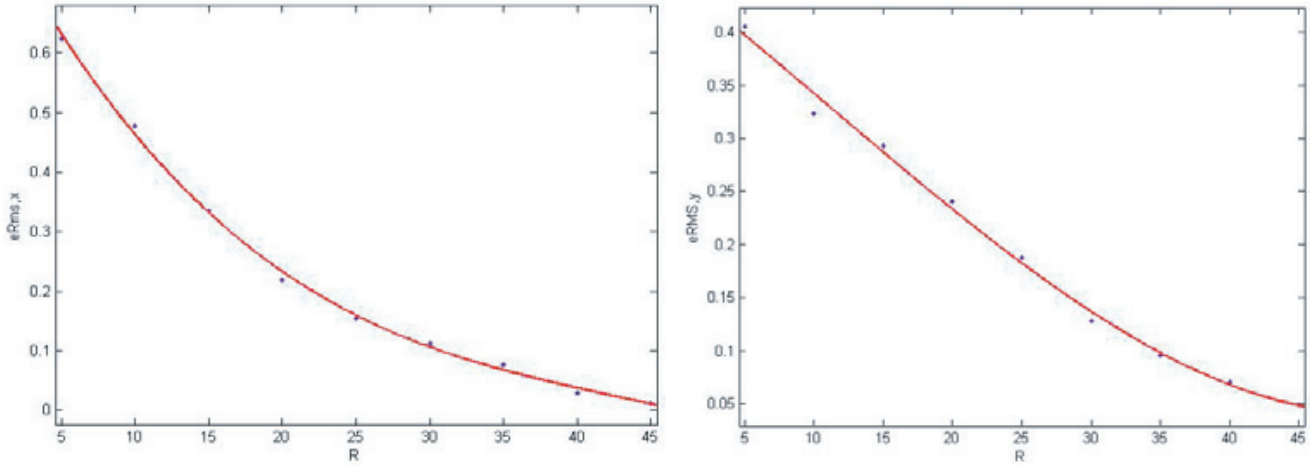

(a) (b)

Figure 15. Tumor target location prediction results of the relation between RMSE and R: (a) abscissa, (b) ordinate.

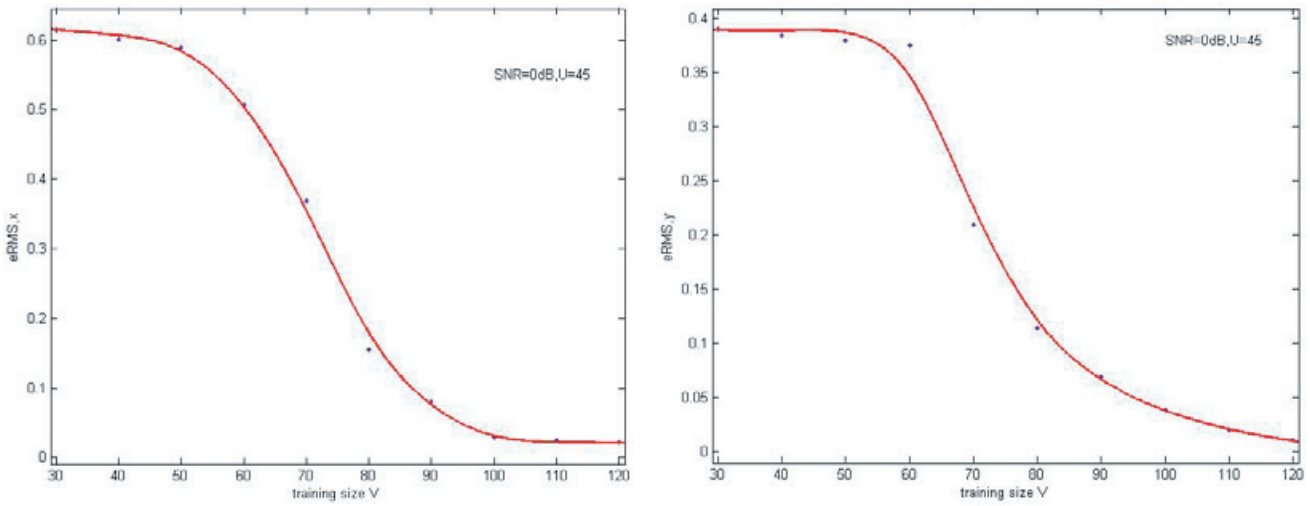

(a) (b)

Figure 16. Tumor target location prediction results of the relation between RMSE and training size V: (a) abscissa, (b) ordinate.

We also studied the prediction error with respect to the training size. The experimental results are shown in Figure 16. It is can be seen that with the increase the size of the training set, ERMS is decreasing.

6. CONCLUSION

This study utilizes the FDTD method to obtain radar signal data. The improved BP algorithm is then employed to calculate the intensity of each pixel in imaging areas. The intensity of each pixel in imaging area and default category labels are marked as the SVM input and output, respectively. Experimental results show that improved BP algorithm can locate tumor targets. However, the BP method produces virtual scenes in multi-target imaging because of signal interference. It is effective to refrain the displacement of image with modifying the time element of BP algorithm by iteration to eliminate virtual scenes The SVM method is applied to select some data as the training set so that the training model can be obtained. The model is used to predict the data with noise pollution, as well as different shapes, quantities, sampling intervals, and sampling distances. The results are satisfactory. The SVM method not only determines the location of tumor targets accurately, but also clearly shows the tumor sizes and shapes. The robustness and feasibility of the method are proved. Future work should focus on improving the efficiency of the proposed method and studying the 3D tumor model.

REFERENCES

1. Bolomey, J. C., "Recent european developments in active microwave imaging for industrial, scientific, and medical applications," *IEEE T. Microw. Theory*, No. 37, pp.2109-2117, Dec. 1989.
2. Caorsi, S., M. Donelli, A. Lommi, and A. Massa, "Location and imaging of two-dimensional scatterers by using a particle swarm algorithm," *Journal of Electromagnetic Waves and Applications*, Vol. 18, No. 4, 481–494, 2004.
3. Craddock, J., M. Donelli, D. Gibbins, and M. Sarafianou, "A three-dimensional time domain microwave imaging method for breast cancer detection based on an evolutionary algorithm," *Progress In Electromagnetics Research M*, Vol. 18, 179–195, 2012.
4. Rocca, P., M. Donelli, G. L. Gragnani, and A. Massa, "Iterative multi-resolution retrieval of non-measurable equivalent currents for the imaging of dielectric objects," *Inverse Problems*, Vol. 25, No. 5, 2009.
5. Franceschini, G., M. Donelli, R. Azaro, and A. Massa, "Inversion of phaseless total field data using a two-step strategy based on the iterative multiscalling approach," *IEEE Transactions on Geoscience and Remote Sensing*, Vol. 44, No. 12, 3527–3539, Dec. 2006.
6. National Breast Cancer Coalition (NBCC), URL: http://www.stopbreast- cancer.org, 2014.
7. Yujiri, L., "Passive millimeter wave imaging," *IEEE MTT-S International Microwave symposium*, Vol. 4, 98–101, Jun. 2006.
8. Hu, C., L. Liu, and B. Sun, "Compact representation and panoramic representation for capsule endoscope images," *Int. J. Inf. Acquisit.*, Vol. 6, 257–268, 2009.
9. Hwang, S. and M. Emre Celebi, "Polyp detection in wireless capsule endoscopy videos based on image segmentation and geometric feature," *Proc. 2010 IEEE Int. Conf. Acoust. Speech Signal Process.*, 678–681, Mar. 2010.
10. Gono, K., "Multifunctional endoscopic imaging system for support of early cancer diagnosis," *IEEE J. Sel. Topics Quant. Electron*, Vol. 14, No. 1, 62–69, Jan. 2008.
11. Gono, K., T. Obi, M. Yamaguchi, N. Ohyama, H. Machida, Y. Sano, S. Yoshida, Y. Hamamoto, and T. Endo, "Appearance of endhanced tissue features in narrow band endoscopic imaging," *J. Biomed. Opt.*, Vol. 9, 568–577, May 2004.
12. Gono, K., K. Yamazaki, N. Doguchi, T. Nonami, T. Obi, M. Yamagichi, N. Ohyama, H. Machida, Y. Saono, S. Yoshida, Y. Hamamoto, and T. Endo, "Endoscopic observation of tissue by narrow band illumination," *Opt. Rev.*, Vol. 10, 211–215, 2003.

13. Atasoy, S., B. Glocker, S. Giannarou, D. Mateus, A. Meining, G. Yang, and N. Navab, "Probabilistic region matching in narrow-band endoscopy for targeted optical biopsy," *Proc. MICCAI*, 499–506, 2009.
14. Li, B. and M. Q.-H. Meng, "Tumor recognition in wireless capsule endoscopy images using textural features and SVM-based feature selection," *IEEE Trans. on Information Technology in Biomedicine*, Vol. 16, No. 3, 323–329, May 2012.
15. Li, B. and M. Q.-H. Meng, "Computer aided detection of bleeding regions in capsule endoscopy images," *IEEE Trans. Biomed. Eng.*, Vol. 56, No. 4, 1032–1039, Apr. 2009.
16. Li, B. and M. Q.-H. Meng, "Texture analysis for ulcer detection in capsule endoscopy images," *Image Vis. Comput.*, Vol. 27, No. 9, 1336–1342, Aug. 2009.
17. Li, B. and M. Q.-H. Meng, "Computer-based detection of bleeding and ulcer in wireless capsule endoscopy images by chromaticity moments," *Comput. Bilo. Med.*, Vol. 39, No. 2, 141–147, Feb. 2009.
18. Wang, L., *Support Vector Machines: Theory and Applications*, Springer-Verlag, New York, 2005.
19. Jain, A. K. and D. Zongker, "Feature selection, evaluation, application, and small sample performance," *IEEE Trans. PAMI*, Vol. 19, No. 2, 153–158, Feb. 1997.
20. Dash, M. and H. Liu, "Feature selection for classification," *Intell. Data Anal.*, Vol. 1, 131–156, 1997.
21. Guyon, I., J. Westion, S. Barnhill, and V. Vapnik, "Gene selection for cancer classification using support vector machines," *Mach. Learn.*, Vol. 46, 389–422, 2002.
22. Wang, F. and Y. Zhang, "A real-time through-wall detection based on support vector machine," *Journal of Electromagnetic Waves and Applications*, Vol. 25, No. 1, 75–84, 2011.
23. Vapnik, V., *The Nature of Statistical Learning Theory*, Springer-Verlag, New York, 1995.
24. Miteran, J., S. Bouillant, and E. Bourennane, "SVM approximation for real-time image segmentation by using an improved hyperrectangles-based method," *Real-Time Imaging*, Vol. 9, 179–188, 2003.
25. Vapnik, V., *Statistical Learning Theory*, J. Wiley, New York, 1998.
26. Steinwart, I., "On the optimal parameter choice for v-support vector machines," *IEEE Trans. on Pattern Analysis and Machine Intelligence*, Vol. 25, No. 10, 1274–1284, 2003.
27. Mangasarian, O. and D. Musicant, "Lagrangian support vector machines," *Journal of Machine Learning Research*, Vol. 1, 161–177, 2001.
28. Salmon, N. A., "Polarimetric scene simulation in millimeter-wave radiometric imaging," *Proc. SPIE*, 260–269, Feb. 2004.
29. Chapelle, O., P. Haffner, V. N. Vapnik, "Support vector machines for histogram-based image classification," *IEEE Transactions on Neural Networks*, Vol. 10, No. 5, 1055–1064, May 1999.
30. Fetterman, M. R., J. Dougherty, and W. L. Kiser, Jr., "Scene simulation of mm-wave images, " *IEEE 2007 AP-S Int. Symposium*, 1493–1496, Dec. 2007.
31. Gurel, L. and U. Oguz, "Three-dimensional FDTD modeling of a ground-penetrating radar," *IEEE Trans. Geosci. Remote Sens.*, Vol. 38, 1513–1520, Apr. 2008.
32. Wu, S. Y., Y. Y. Xu, and J. Chen, "Through-wall shape estimation based on UWB-SP radar," *IEEE Geosci. Remote Sens. Letters*, Vol. 10, 1234–1238, May 2013.
33. Dehmollaian, M., "Through-wall shape reconstruction and wall parameters estimation using differential evolution," *IEEE Geosci. Remote Sens. Letters*, Vol. 8, 201–205, Feb. 2011.
34. Cheng, Z., W. Ji, and L. Hao, "Imaging algorithm for synthetic aperture interferometric radiometer in near field," *Science China Technological Sciences*, Vol. 54, 2224–2231, Aug. 2011.
35. Lei, W., C. Huang, and Y. Su, "A real-time BP imaging algorithm in SPR application," *IEEE International Geoscience and Remote Sensing Symposium*, 1734–1737, 2005.
36. Ahmad, F., M. Amin, and S. Kassam, "A beamforming approach to stepped-frequency synthetic aperture through-the-wall radar imaging," *IEEE International Workshop on Computational Advances in Multi-Sensor Adaptive Processing*, 24–27, 2005.